International Journal of General Medicine

Dovepress
open access to scientific and medical research

Open Access Full Text Article

ORIGINAL RESEARCH

Combined CT-Based Radiomics and Clinic-Radiological Characteristics for Preoperative Differentiation of Solitary-Type Invasive Mucinous and Non-Mucinous Lung Adenocarcinoma

Rong Hong[1,2,*], Xiaoxia Ping[2,3,*], Yuanying Liu[2], Feiwen Feng[2], Su Hu[2,3], Chunhong Hu[2,3]

[1]Department of Radiology, Suzhou TCM Hospital Affiliated to Nanjing University of Chinese Medicine, Suzhou, Jiangsu, 215100, People's Republic of China; [2]Department of Radiology, the First Affiliated Hospital of Soochow University, Suzhou, Jiangsu Province, 215006, People's Republic of China; [3]Institute of Medical Imaging, Soochow University, Suzhou, Jiangsu, 215006, People's Republic of China

*These authors contributed equally to this work

Correspondence: Chunhong Hu; Su Hu, Department of Radiology, The First Affiliated Hospital of Soochow University; Institute of Medical Imaging, Soochow University, Suzhou, Jiangsu, People's Republic of China, Email sdhuchunhong@sina.com; husu@suda.edu.cn

Purpose: The clinical, pathological, gene expression, and prognosis of invasive mucinous adenocarcinoma (IMA) differ from those of invasive non-mucinous adenocarcinoma (INMA), but it is not easy to distinguish these two. This study aims to explore the value of combining CT-based radiomics features with clinic-radiological characteristics for preoperative diagnosis of solitary-type IMA and to establish an optimal diagnostic model.

Methods: In this retrospective study, a total of 220 patients were enrolled and randomly assigned to a training cohort (n = 154; 73 IMA and 81 INMA) and a testing cohort (n = 66; 31 IMA and 35 INMA). Radiomics features and clinic-radiological characteristics were extracted from plain CT images. The radiomics models for predicting solitary-type IMA were developed by three classifiers: linear discriminant analysis (LDA), logistic regression-least absolute shrinkage and selection operator (LR-LASSO), and support vector machine (SVM). The combined model was constructed by integrating radiomics and clinic-radiological features with the best performing classifier. Receiver operating characteristic (ROC) curves were used to evaluate models' performance, and the area under the curve (AUC) were compared by the DeLong test. Decision curve analysis (DCA) was conducted to assess the clinical utility.

Results: Regarding CT characteristics, tumor lung interface, and pleural retraction were the independent risk factors of solitary-type IMA. The radiomics model using the SVM classifier outperformed the other two classifiers in the testing cohort, with an AUC of 0.776 (95% CI: 0.664–0.888). The combined model incorporating radiomics features and clinic-radiological factors was the optimal model, with AUCs of 0.843 (95% CI: 0.781–0.906) and 0.836 (95% CI: 0.732–0.940) in the training and testing cohorts, respectively.

Conclusion: The combined model showed good ability in predicting solitary-type IMA and can provide a non-invasive and efficient approach to clinical decision-making.

Keywords: computed tomography, invasive mucinous adenocarcinoma, radiomics, machine learning

Introduction

Lung cancer is a major contributor to cancer-related deaths, with adenocarcinoma being the most predominant subtype.[1] Invasive mucinous adenocarcinoma (IMA) is a unique variant of lung adenocarcinoma, less common than invasive non-mucinous adenocarcinoma (INMA), accounting for approximately 2–5% of lung adenocarcinoma.[2,3] IMA and INMA are two distinct entities. As the name suggests, IMA is characterized as abnormal intracytoplasmic mucin production by columnar and goblet cells, which is rarely observed in INMA.[4] Additionally, IMA exhibits distinct molecular features,

Received: 19 July 2024
Accepted: 11 September 2024
Published: 21 September 2024

with KRAS mutations being the most frequent oncogenic driver mutation (63% to 90%), followed by NRG1 fusions and ERBB2.[4–6] However, EGFR mutations, the most common oncogenic driver mutation in INMA, are notably rare in IMA. The recurrence rate of intrapulmonary IMA is higher than that of INMA, which is associated with a higher incidence of the spread through air spaces (STAS).[7,8] These distinct characteristics of IMA necessitate different treatment approaches compared to INMA. The precise clinical diagnosis of IMA is essential for guiding treatment and predicting the prognosis of patients. Due to the cytologic usually inconspicuous or absent atypia, definitive diagnosis of IMA through biopsy is normally challenged.[9] In contrast, computed tomography (CT) offers a non-invasive examination technique that provides a comprehensive and direct overview of the entire tumor.

The common clinical symptoms of IMA include cough, chest pain, and chest congestion.[10,11] Coughing up with white, foamy sputum occurs more frequently in INMA and can sometimes be the primary symptom of IMA. These clinical manifestations lack specificity, as more than half of patients with IMA are asymptomatic at the time of their initial diagnosis, with the majority of IMA lesions detected during routine CT screening.[11,12] Radiologically, IMAs can present as either solitary-type or pneumonic-type based on CT findings.[13,14] The solitary-type is defined as a solitary nodule or mass with a defined shape. The solitary-type is the most common radiological morphology of IMA (79.4–81.9%),[10,11] while pneumonic-type is considered as a progressive period of solitary-type.[14,15] Solitary-type IMA has diverse imaging features, including lobulated or spiculated margin, bubblelike vacuole or cavitation, air bronchogram, and pleural retraction, as reported in previous studies.[10,14,16–18] However, these CT features lack specificity and can also be observed in INMA, which impedes the identification of solitary-type IMA.

Conventional CT images contain a large amount of useful information that is often not fully utilized. Radiomics can extract morphological and pathophysiological quantitative information of tumors from CT images, which are closely linked to clinical outcomes in the field of oncology management.[19] In the re-grading of lung cancer, CT-based radiomics serves as a practical and cost-effective tool commonly employed to differentiate between benign and malignant lung nodules and assess the degree of invasiveness of lung adenocarcinoma.[20,21] Machine learning is a sub-field of artificial intelligence. Traverso et al[22] proposed that machine learning-based radiomics can help construct robust predictive models. Thus, in this study, we aim to develop and validate radiomics models using machine learning algorithms. Additionally, we investigate the potential enhancement in discrimination of solitary-type IMA by integrating clinic-radiological and radiomics features into a combined model, as opposed to utilizing either the clinical or radiomics model independently.

Materials and Methods

Patients

The clinical and imaging data of patients with lung adenocarcinoma in our hospital between December 2015 to July 2022 were retrospectively analyzed. The inclusion criteria as follows: (1) availability of thin-section chest CT examination within 2 weeks before surgery; (2) pathologically confirmed IMA and INMA. The exclusion criteria as follows: (1) pneumonic-type IMA presenting on CT images; (2) pathologically proved mixed invasive mucinous/non-mucinous adenocarcinoma (≥ 10% of both non-mucinous and mucinous component); (3) history of antitumor therapy before CT examination, such as radiotherapy or chemotherapy; (4) incomplete clinical and imaging data. A total of 220 patients (75 males and 145 females, mean age 61 years, ranging from 28 to 84) were enrolled in this study, including 104 cases of IMA and 116 cases of INMA. This study was approved by the institutional review board of the First Affiliated Hospital of Soochow University. Informed written consent was waived due to the retrospective nature and the utilization of de-identified data. The study was conducted in accordance with the Declaration of Helsinki (as revised in 2013).

The patients were randomly assigned to a training cohort (IMA, n = 73; INMA, n = 81) and a testing cohort (IMA, n = 31; INMA, n = 35) in a 7:3 ratio. All cases in the training cohort were used to train the prediction model, while cases in the testing cohort were utilized to assess the model's performance independently. Clinical and radiological features were collected for analysis, including gender, age, maximum diameter of the lesion displayed by MPR lung window setting, tumor density (solid or subsolid), shape (round/oval or irregular), tumor lung interface (obscure or clear), presence of lobulation, spiculation, pleural retraction, air bronchogram, lower lobe involvement, and presence of air-

containing space like bubblelike vacuole or cavitation.[17] All features were independently assessed by two radiologists (6 and 14 years of experience in thoracic CT imaging diagnosis, respectively) using the Picture Archiving and Communication System (PACS). Any disagreements were resolved through discussion. Furthermore, the largest lesion with pathologic result was selected for analysis when multiple lesions were present.

Pathologic Evaluation

The slides of the resected specimens were formalin-fixed, paraffin-embedded, and stained with hematoxylin and eosin (H&E). Based on the WHO classification of lung adenocarcinoma, invasive adenocarcinoma is defined as pure mucinous type adenocarcinoma (mucinous component ≥ 90%), mixed mucinous/non-mucinous type adenocarcinoma (both non-mucinous and mucinous component ≥ 10%), and non-mucinous adenocarcinoma (minimal mucinous component < 10%).[2,3] Pure mucinous adenocarcinoma was enrolled as IMA in this present study. The pathologic evaluation was performed by two pathologists who was experienced in pulmonary pathologic analysis.

Image Acquisition

All the chest CT examinations were performed with multidetector CT scanners: Philips Healthcare (Brilliance 16, Brilliance iCT, IQON spectral CT), Siemens Healthineers (Somatom Sensation 64, Somatom Definition), GE Healthcare (GE revolution, Discovery CT 750 hD), Toshiba Medical System (Aquilion One). The CT scanning parameters were as follows: tube voltage, 100 to 120 kVp; automatic tube current; rotation time, 0.5 or 0.8s; detector collimation, 128×0.6 or 64×0.625 mm; slice thickness, 0.5–1.25 mm; reconstruction interval, 1–2.5 mm; matrix of 512×512 mm. The CT images were acquired in the supine position with deep inspiratory breath-hold.

Tumor Segmentation

CT images were downloaded from PACS, anonymized, and then exported into 3D Slicer software (version 4.10.2). Tumor segmentation was performed by a radiologist with 6 years of experience in thoracic CT imaging diagnosis. The volume of interest (VOI) was manually contoured along the boundary of the tumor slice-by-slice with the lung window settings. Subsequently, another radiologist with 14 years of experience in thoracic CT imaging diagnosis confirmed the VOIs. All observers were blinded to the clinical and pathologic diagnosis. After four weeks, thirty patients were randomly selected for the evaluation of intra-observer and inter-observer reproducibility of the extracted radiomics features using intraclass correlation coefficient (ICC), with consistency considered good when ICC > 0.80.[23]

Radiomics Feature Extraction and Selection

We use the PyRadiomics platform to extract radiomics features, including first-order, shape, and texture features like gray level co-occurrence matrix (GLCM) features, gray level size zone matrix (GLSZM) features, gray level run length matrix (GLRLM) features, neighboring gray tone difference matrix (NGTDM) features, and gray level dependence matrix (GLDM) features. First and texture features were also calculated through filters, including wavelet, Laplacian of Gaussian (LoG), square, square root, logarithm, exponential, gradient, and local binary pattern (LBP).

The whole radiomics analysis process was conducted using the open-source software FeAture Explorer Pro (FAE, version 0.5.2).[24] The workflow of radiomics analysis is presented in Figure 1. First, upsampling was used to balance the positive and negative samples in the training set. Next, the z-score normalization method was applied to each radiomics feature by subtracting and dividing the mean value by the standard deviation. Subsequently, the Pearson correction coefficient (PCC) was employed to reduce the dimensions of the feature matrix by comparing the similarity of each pair of features and removing one of the highly correlated features (PCC > 0.99). Finally, recursive feature elimination (RFE) was employed to select relevant features by iteratively removing the least important ones based on the classifier, with the number of features ranging from 1 to 20.

Models' Construction and Evaluation

Based on the selected radiomics features, three common machine learning classifiers, linear discriminant analysis (LDA), logistic regression-least absolute shrinkage and selection operator (LR-LASSO), and support vector machine (SVM)

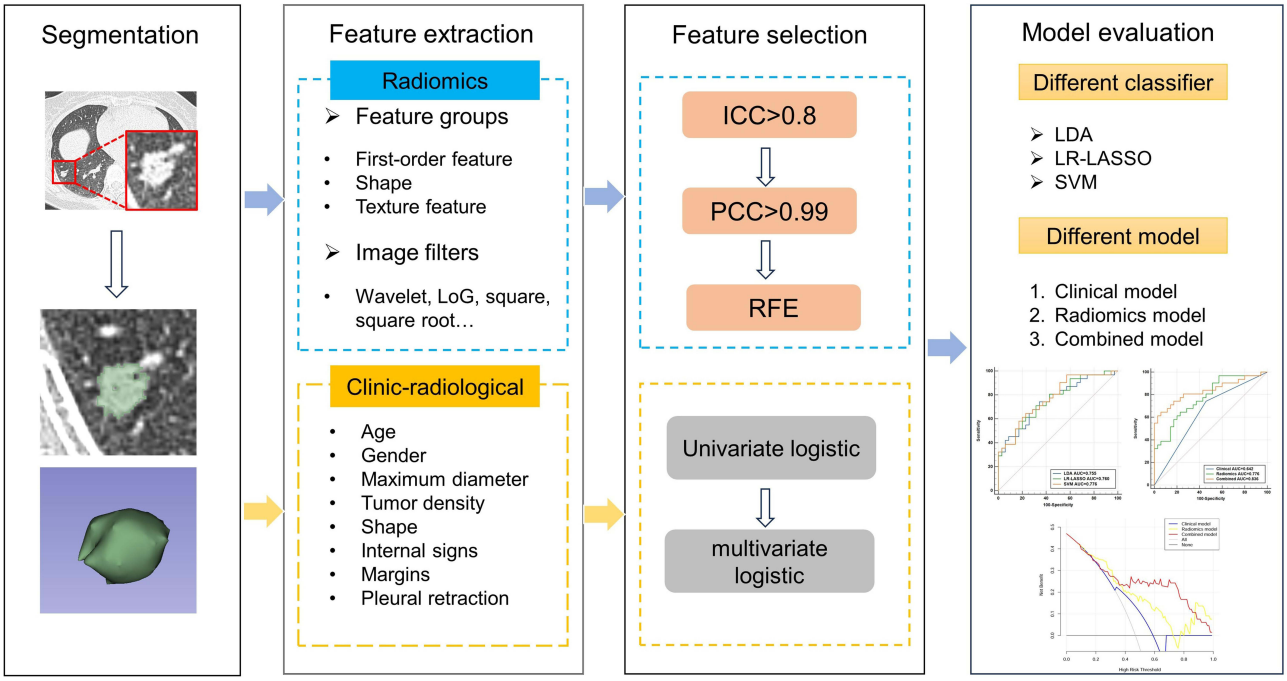

Figure 1 The workflow of this study.

were utilized to construct radiomics models. The training cohort underwent hyperparameter optimization by using 5-fold cross-validation. In 5-fold cross-validation, the entire dataset was randomly separated into five subsets. When one subset was used as a testing set, the other four groups were used as training set. The training-testing procedures were repeated five times until each sample in the dataset was used as a training and testing sample once. The best radiomics model was determined by comparing metrics including area under the curve (AUC) from the receiver operating characteristic (ROC) curve, accuracy (ACC), sensitivity (SEN), specificity (SPE), positive predictive value (PPV), negative predictive value (NPV).

Univariate and multivariate logistic regression analysis were applied to select independent clinic-radiological factors, which were subsequently used to develop a combined model. Based on the training set, we compared the clinic-radiological features selected by logistic regression analysis and the radiomics features obtained through RFE. Features with high correlation (PCC > 0.99) were removed, and the remaining features were then utilized to construct a combined model using the machine learning classifier that performed best in the radiomics model. In addition, a clinical model was constructed based on clinic-radiological factors. All models' performances were evaluated in the training and testing cohort using the ROC curve and quantified by the area under the curve (AUC). Decision curve analysis (DCA) was conducted to assess the clinical utility of the three models.

Statistical Analysis

All statistical analyses were performed using the SPSS software (version 25.0, IBM Corp, Armonk, NY) and R software (version 4.1.0; https://www.r-project.org/). Numerical variables were expressed as means ± standard deviations or medians and interquartile ranges and compared by the Student's *t*-test or the Mann–Whitney *U*-test. Categorical variables are expressed as percentages, and analyzed by chi-square test. After identifying statistically significant clinic-radiological variables in univariate analyses, we included them in multivariate logistic regression analyses and screened for independent risk factors predictive of solitary-type IMA by using a forward stepwise selection method. The AUC values of the models were compared by the DeLong test. The calibration curve was used to assess the calibration ability of the combined model. A two-sided *P* value < 0.05 was considered statistically significant.

Results

Patient Basic Characteristics

A total of 220 patients (104 cases of IMA and 116 cases of INMA) were enrolled and randomly assigned to the training and testing cohort at a 7:3 ratio. The training cohort consisted of 73 (47.4%) IMA patients and 81 (52.6%) INMA patients, while the testing cohort had 31 (47.0%) IMA patients and 35 (53.0%) INMA patients. As shown in Table 1, the clinic-radiological features of the two cohorts were well-balanced, supporting the rationale of the patient grouping. The median diameter of the IMA group in the training cohort was 12.95mm (IQR: 9.03–19.63), which was significantly smaller than that of the INMA group with a median diameter of 19.35mm (IQR: 13.33–24.58). The difference of diameter between the two groups in the testing cohort was also statistically significant ($P < 0.05$). In terms of location, 40 (54.8%) IMAs and 23 (28.4%) INMAs were found in the lower lobe of the lung in the training set, showing a significant statistical difference. Moreover, characteristics such as tumor lung interface, lobulation, and pleural retraction were

Table 1 Clinical and Radiological Characteristics of Patients in the Training and Testing Cohorts

Characteristics	Training Cohort (n=154)			Testing Cohort (n=66)			#P
	INMA (n=81)	IMA (n=73)	P	INMA (n=35)	IMA (n=31)	P	
Age (years, mean ± SD)	62.47±9.61	60.40±11.26	0.220	63.63±9.94	58.81±10.75	0.063	0.936
Max diameter (mm, IQR)	19.35 (13.33,24.58)	12.95 (9.03,19.63)	<0.001	19.65 (14.70,28.4)	9.95 (8.75,15.7)	0.001	0.804
Gender, n (%)			0.234			0.967	0.277
Female	48(59.3%)	50(68.5%)		25(71.4%)	22(71.0%)		
Male	33(40.7%)	23(31.5%)		10(28.6%)	9(29.0%)		
Solidity, n (%)			0.801			0.948	0.099
Sub-solid	24(29.6%)	23(31.5%)		7(20.0%)	6(19.4%)		
Solid	57(70.4%)	50(68.5%)		28(80.0%)	25(80.6%)		
Shape, n (%)			0.058			0.179	0.858
Round or oval	41(50.6%)	48(65.8%)		18(51.4%)	21(67.7%)		
Irregular	40(49.4%)	24(34.2%)		17(48.6%)	10(32.3%)		
Tumor lung interface, n (%)			<0.001			0.014	0.906
Obscure	29(35.8%)	47(64.4%)		12(34.3%)	20(64.5%)		
Clear	52(64.2%)	26(35.6%)		23(65.7%)	11(35.5%)		
Lobulation, n (%)			0.001			<0.001	0.423
No	13(16.0%)	30(41.1%)		2(5.7%)	13(41.9%)		
Yes	68(84.0%)	43(58.9%)		33(94.3%)	18(58.1%)		
Spiculation, n (%)			0.051			0.030	0.711
No	64(79.0%)	66(90.4%)		27(77.1%)	30(96.8%)		
Yes	17(21.0%)	7(9.6%)		8(22.9%)	1(3.2%)		
Pleural retraction, n (%)			<0.001			0.019	0.185
No	25(30.9%)	51(69.9%)		16(45.7%)	23(74.2%)		
Yes	56(69.1%)	22(30.1%)		19(54.3%)	8(25.8%)		
Air bronchogram, n (%)			0.068			0.383	0.805
No	58(71.6%)	42(57.5%)		25(71.4%)	19(61.3%)		
Yes	23(28.4%)	31(42.5%)		10(28.6%)	12(38.7%)		
Air-containing space, n (%)			0.076			0.816	0.198
No	68(84.0%)	68(93.2%)		29(82.9%)	25(80.6%)		
Yes	13(16.0%)	5(6.8%)		6(17.1%)	6(19.4%)		
Lower lobe, n (%)			0.001			0.024	0.097
No	58(71.6%)	33(45.2%)		21(60.0%)	10(32.3%)		
Yes	23(28.4%)	40(54.8%)		14(40.0%)	21(67.7%)		

Notes: #P means the comparison between the training set and the testing set. n (%) represents categorical variables were reported as frequency and proportions.

Abbreviations: SD, standard deviation; IQR, interquartile range; INMA, invasive non-mucinous adenocarcinoma; IMA, invasive mucinous adenocarcinoma.

significantly different between the IMA and INMA groups (all $P < 0.05$). The remaining characteristics between the two groups showed no significant difference.

Clinic-Radiological Features Screening and Model Development

The univariate logistic analysis revealed that the tumor lung interface, lobulation, pleural retraction, and lower lobe were significantly associated with IMA in the training cohort. The following multivariate logistic analysis showed that the tumor lung interface (OR = 3.483; 95% CI: 1.647–7.365; $P = 0.001$) and pleural retraction (OR = 4.285; 95 CI%: 2.003–9.166; $P < 0.001$) were the independent risk factors of IMA (Table 2). The following clinical model was developed using these two features.

Radiomics Feature Selection and Radiomics Model Development

Among the extracted radiomics features, 87.9% of features had good consistency (interobserver ICC ≥ 0.80), indicating good reliability of the radiomics features. Following feature reduction and selection, seven optimal radiomics features (one first-order feature and six texture features) were chosen for further analysis (Table 3). These selected radiomics features showed low correlation coefficients (Figure 2), which were employed in the construction of radiomics models for diagnosing IMA. The performance of radiomics models based on LDA, LR-LASSO, and SVM classifiers in both the training and testing cohorts is presented in Figure 3 and Table 4. Among all the radiomics models in the testing cohort, the SVM model showed the best performance, with an AUC of 0.776 (95% CI: 0.664–0.888), an accuracy of 0.697, a sensitivity of 0.613, and a specificity of 0.771. The radiomics model using the SVM classifier had the highest AUC

Table 2 Univariate and Multivariable Logistic Regression Analyses for Selecting Clinical Radiological Features

Variable	Univariate Analysis		Multivariate Analysis	
	OR (95% CI)	*P*	OR (95% CI)	*P*
Age	0.981(0.951–1.012)	0.220		
Gender	1.495(0.770–2.902)	0.235		
Max diameter	0.975(0.944–1.007)	0.119		
Solidity	1.092(0.550–1.171)	0.801		
Shape	1.873(0.977–3.591)	0.059		
Tumor lung interface	3.241(1.675–6.272)	<0.001	3.483(1.647–7.365)	0.001
Lobulation	3.649(1.716–7.761)	0.001	2.010(0.837–4.824)	0.118
Spiculation	2.504(0.973,6.443)	0.057		
Pleural retraction	5.193(2.612–10.323)	<0.001	4.285(2.003–9.166)	<0.001
Air bronchogram	0.537(0.275–1.050)	0.069		
Air-containing space	2.600(0.879–7.693)	0.084		
Lower lobe	0.327(0.168–0.638)	0.001	0.467(0.218–1.002)	0.051

Abbreviations: OR, odd ratio; CI, confidence interval.

Table 3 Selected Features of Radiomics Model and Combined Model

Radiomics Model	Combined Model
Lung_exponential_gldm_dependencevariance	Lung_exponential_gldm_dependencevariance
Lung_lbp-2D_gldm_smalldependencehighgraylevelemphasis	Lung_lbp-2d_gldm_smalldependencehighgraylevelemphasis
Lung_log-sigma-5-0-mm-3D_glszm_sizezonenonuniformitynormalized	Lung_original_glrlm_shortrunlowgraylevelemphasis
Lung_original_glrlm_shortrunlowgraylevelemphasis	Lung_wavelet-hhl_glcm_correlation
Lung_wavelet-HHH_glcm_Correlation	Pleural_retraction
Lung_wavelet-HHL_glcm_Correlation	Tumor_lung_interface
Lung_wavelet-HLL_firstorder_Skewness	

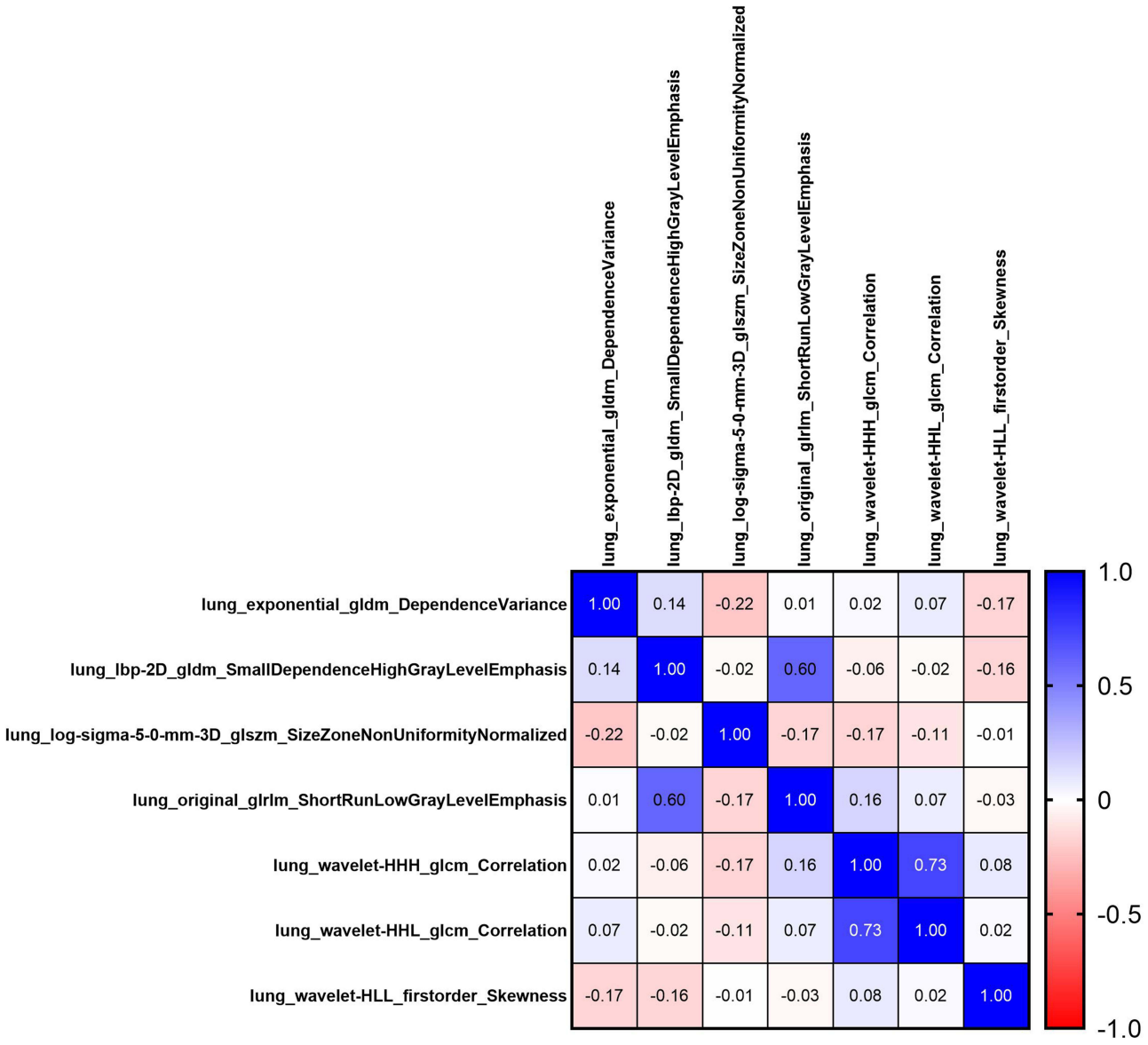

Figure 2 Radiomics heatmap. Heatmap describing the correlation coefficient matrices of seven selected radiomics features.

compared to the other two classifiers, LDA and LR-LASSO (all $P > 0.05$). Therefore, the SVM classifier was chosen as the machine learning algorithm for developing the radiomics model in this study.

Combined Model Construction and Validation

We constructed the combined model by integrating the clinic-radiological features selected through multivariate logistic regression analysis with the radiomics features obtained through RFE (Table 3). To uniformly and objectively assess diagnostic performance, we constructed the clinical model, radiomics model, and combined model using SVM classifier. The results of the ROC curve analysis for predicting IMA are illustrated in Figure 4. Detailed statistics of the diagnostic efficacy in the three models are summarized in Table 5. The combined model showed the best discriminative ability in both training and testing sets, with AUC values of 0.843 and 0.836, respectively. In the testing set, the combined model, with the best predictive efficacy (AUC = 0.836, 95% CI: 0.732–0.940), was superior to the radiomics model (AUC = 0.776, 95% CI: 0.664–0.888, $P = 0.149$) and the clinical model (AUC = 0.642, 95% CI: 0.528–0.757, $P = 0.003$). There was no significant difference between the clinical model and the radiomics model in the testing cohort ($P = 0.102$). The

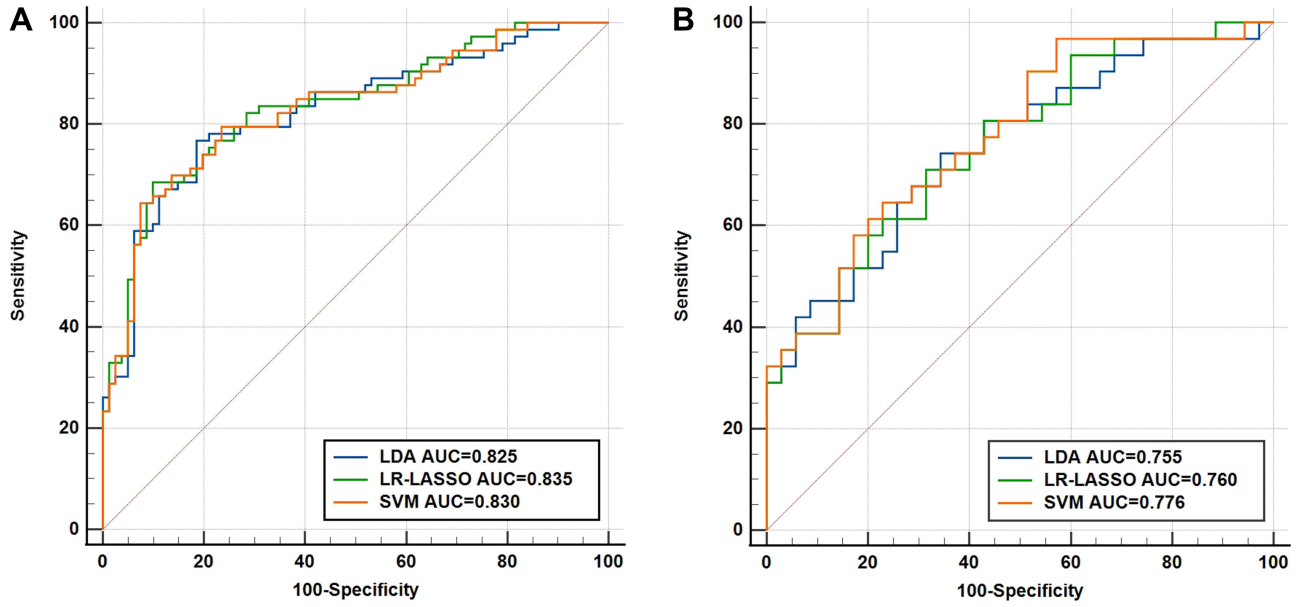

Figure 3 The receiver operating characteristic (ROC) curves of the LDA, LR-LASSO, and SVM in the training (**A**) and testing (**B**) cohorts.

calibration curve demonstrated a good concordance between prediction and observation of the combined model (Figure 5), and the Hosmer-Lemeshow test indicated good calibration of the combined model in both the training and testing sets (P = 0.598; P = 0.522). Furthermore, DCA curve analysis revealed that the combined model provided a higher clinical benefit when compared to the clinical and radiomics models, with the threshold probability range of 0.35 to 0.9 (Figure 6).

Discussion

In this study, we developed and validated CT-based radiomics model for distinguishing solitary-type IMA and INMA. The results showed that the radiomics model had good discriminatory efficacy, especially when combined with clinic-radiological predictors. Therefore, a combined model was constructed based on radiomics features and clinic-radiological predictors, which yielded the best predictive performance for solitary-type IMA, with AUCs of 0.843 (95% CI: 0.781–0.906) and 0.836 (95% CI: 0.732–0.940) in training and testing sets, respectively. Furthermore, compared to radiomics and clinical models, the combined model showed improved accuracy, sensitivity, and specificity, offering valuable information for clinicians to develop personalized treatment plans.

As a distinct pathological type of lung adenocarcinoma, IMA presents unique clinical, pathological, and prognostic characteristics compared to INMA. The definitive diagnosis of IMA usually requires invasive biopsy or post-surgical

Table 4 Predictive Ability of Models Using Different Machine Learning Classifiers

Model		AUC (95% CI)	ACC	SEN	SPE	PPV	NPV
LDA	Training	0.825(0.758–0.892)	0.792	0.767	0.815	0.789	0.795
	Testing	0.755(0.637–0.872)	0.697	0.677	0.714	0.677	0.714
LR-LASSO	Training	0.835(0.770–0.900)	0.792	0.671	0.901	0.860	0.753
	Testing	0.760(0.645–0.875)	0.682	0.581	0.771	0.692	0.675
SVM	Training	0.830(0.765–0.896)	0.786	0.699	0.864	0.823	0.761
	Testing	0.776(0.664–0.888)	0.697	0.613	0.771	0.704	0.692

Abbreviations: AUC, area under the curve; CI, confidence interval; ACC, accuracy; SEN, sensitivity; SPE, specificity; PPV, positive prediction value, NPV, negative prediction value; LDA, linear discriminant analysis; LR-LASSO, logistic regression-least absolute shrinkage and selection operator; SVM, support vector machine.

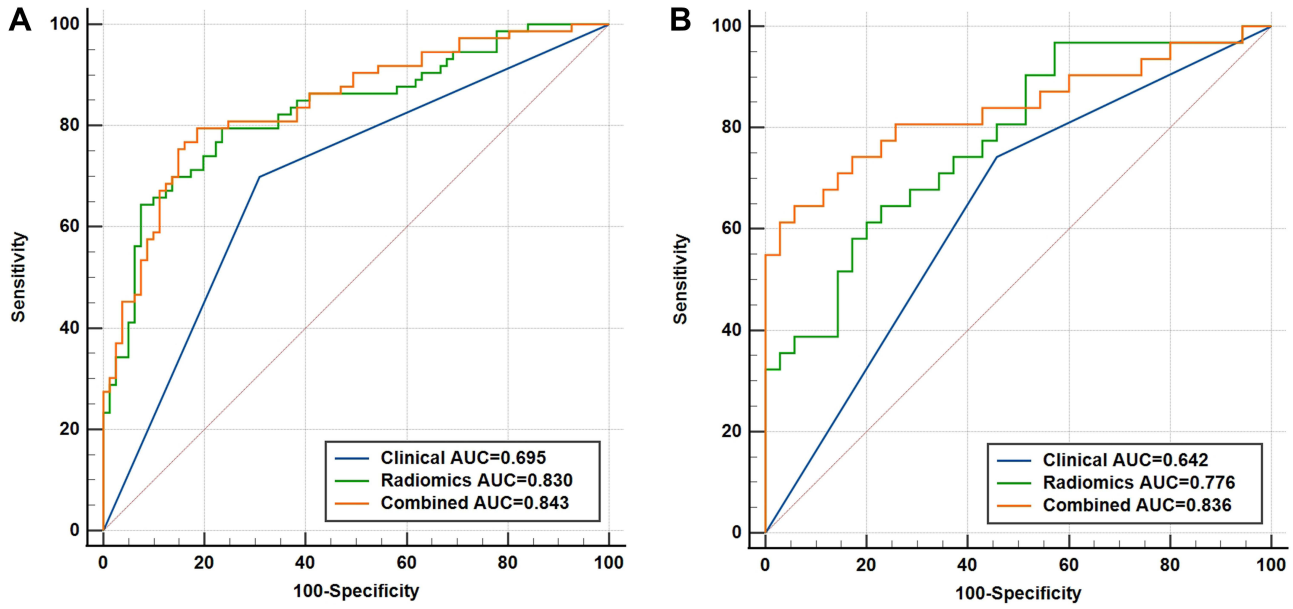

Figure 4 ROC curves of the clinical model, radiomics model, and combined model for differentiating solitary-type IMA and INMA in the training cohort (**A**) and testing cohort (**B**).

pathology, both of which are often challenged. Radiomics, a novel noninvasive diagnostic method, captures the underlying heterogeneity of tumors and serves as an alternative to tissue biopsy in specific settings, providing more information on the internal characteristics of tumors.[19,25] Radiomics has shown significant advantages in predicting lung cancer phenotypes, identifying immunotherapy-related biomarkers, and diagnosing immune checkpoint inhibitor-related pneumonitis.[26–28] Prior studies have highlighted the benefits of the radiomics approach in the diagnosis of IMA.[29,30] Kakino et al[31] have proposed that the contrast enhancement of contrast images may affect some radiomics features and their variability when compared to non-contrast CT images. Thus, different from the approach taken by Zhang et al,[29] we develop the model focusing on extracting radiomics features from the plain CT image. The AUC of our radiomics model was found to be comparable to the model created by Zhang et al,[29] which indicated that the radiomics model based on plain CT images was equally effective in distinguishing between IMA and INMA. Previous studies have shown that machine learning algorithms can improve the diagnostic performance of models.[32–35] In this study, we utilized different algorithms to optimize radiomics analysis for the improvement of stability and generalization. We assessed the performance of various classifiers in distinguishing IMA and INMA, and the results indicated that the SVM

Table 5 Predictive Performance of Three Models in the Training and Testing Cohort

Model	AUC (95% CI)	ACC	SEN	SPE	PPV	NPV
Training cohort						
Clinical	0.695(0.622–0.768)	0.695	0.699	0.691	0.671	0.718
Radiomics	0.830(0.765–0.896)	0.786	0.699	0.864	0.823	0.761
Combined	0.843(0.781–0.906)	0.799	0.781	0.815	0.792	0.805
Testing cohort						
Clinical	0.642(0.528–0.757)	0.636	0.742	0.543	0.590	0.704
Radiomics	0.776(0.664–0.888)	0.697	0.613	0.771	0.704	0.692
Combined	0.836(0.732–0.940)	0.773	0.807	0.743	0.735	0.813

Abbreviations: AUC, area under the curve; CI, confidence interval; ACC, accuracy; SEN, sensitivity; SPE, specificity; PPV, positive prediction value; NPV, negative prediction value.

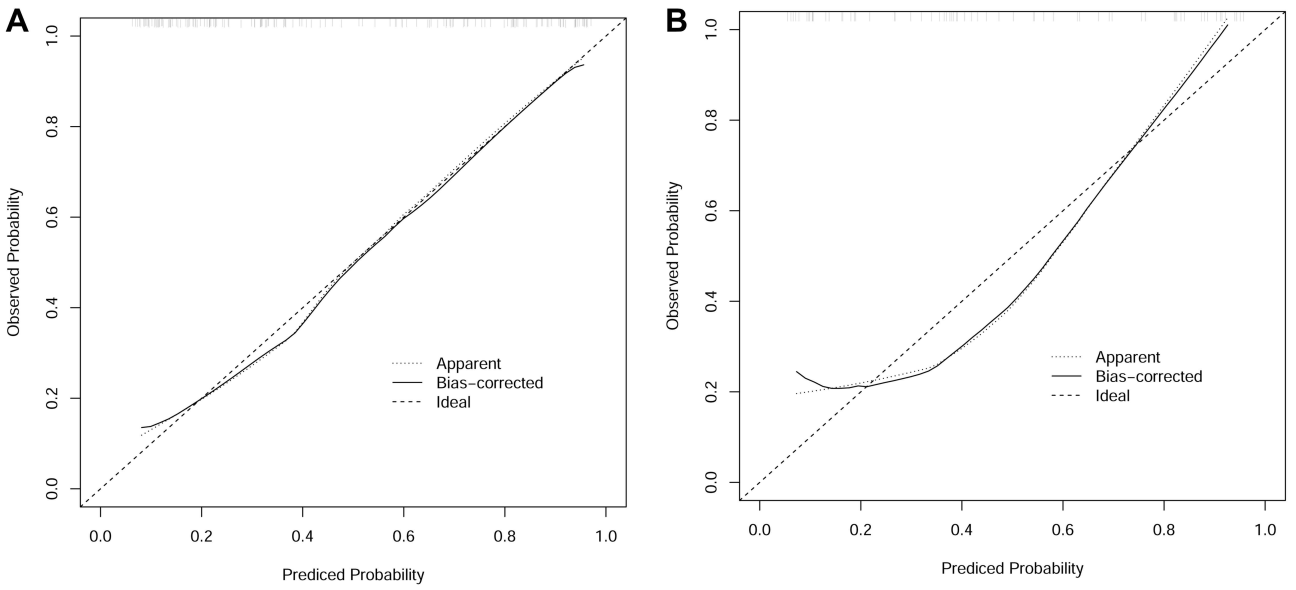

Figure 5 The calibration curve of the combined model in the training (**A**) and testing (**B**) sets.

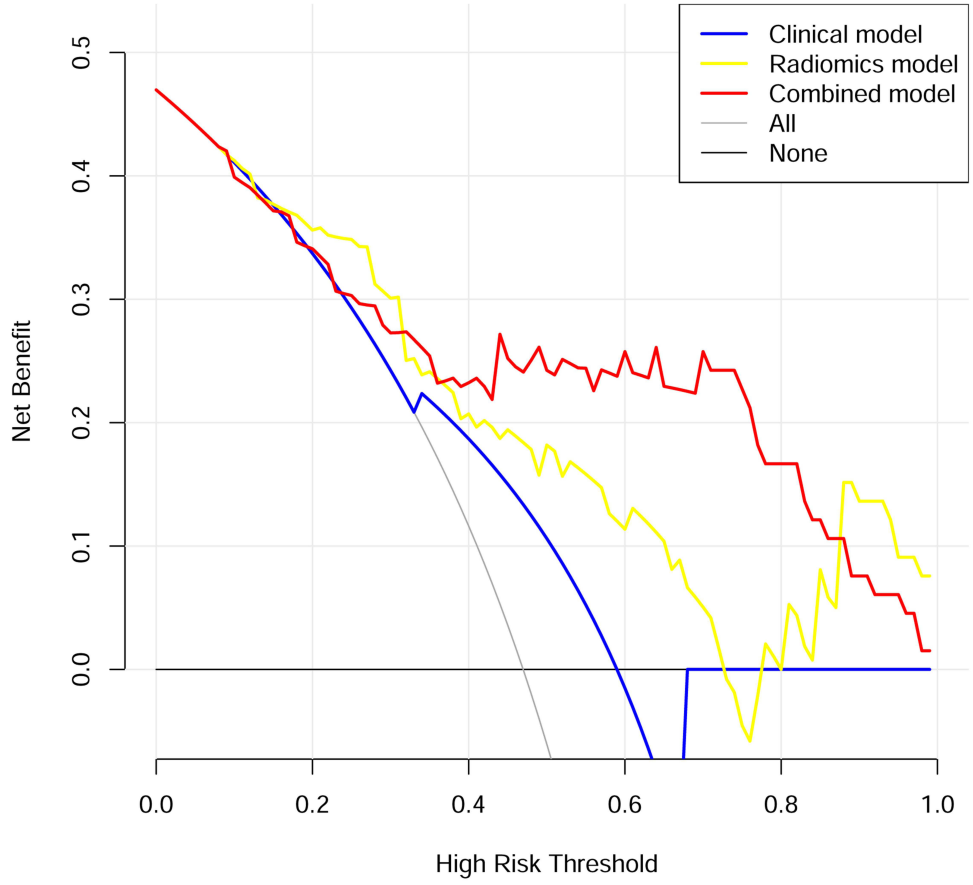

Figure 6 Decision curve analysis (DCA) for three models in the testing cohort. The curves indicated that the combined model had a higher clinical benefit when compared to the clinical and radiomics models, with a threshold probability range of 0.35 to 0.9.

classifier was the best for developing the radiomics model. The SVM is a widely used and robust classifier for classified tasks, even when confronted with limited data availability.[36]

Consistent with previous research,[10,18] we found that CT features such as tumors located in the lower lobe of the lung, tumor lung interface, lobulation, and pleural retraction were tightly associated with pulmonary solitary-type IMA. Furthermore, multivariate logistic regression analysis in our study revealed that the tumor lung interface (OR = 3.483; 95% CI: 1.647–7.365) and pleural retraction (OR = 4.285; 95% CI: 2.003–9.166) were the independent predictors for solitary-type IMA. Unlike INMA, the characterization of IMA were the mixture of mucin accumulation and invasive tumor lesions. When excessive mucus within the lesion overflowed into the surrounding alveolar cavity, it would cause an indistinct and irregular interface.[16] IMA tumors primarily consist of mucin accumulation and rarely surrounding desmoplastic reaction, which accounts for the reduced occurrence of contractive signs like spiculation and pleural retraction in IMA. Zhang et al[18] have found that lesion solidity and the presence of air bronchogram or vacuolar signs were the independent influencing factors of IMA. However, these characteristics did not show significant statistical differences in our study, which could be attributed to the sample size.

In this study, the majority of radiomics features selected for modeling are high-order features that obtained through filters, which can eliminate noise in the original image or sharpen the original image while maintaining the same semantic meaning of features.[37] Some studies found that filters may potentially help discern and amplify differences in radiomics-related metrics.[38,39] According to that, we proposed that higher-order texture features could potentially offer improved discrimination between IMA and INMA. Our ROC analyses revealed that the AUC values for the radiomics model were 0.830 in the training set and 0.776 in the testing set. By integrating clinic-radiological factors with radiomics features, the combined model demonstrated superior performance compared to both the clinical and radiomics models, while also demonstrating high sensitivity and specificity. This improvement may be attributed to the comprehensive information contained within radiomics features, while CT morphological features provide a valuable addition that enhances the predictive performance of the combined model. Furthermore, the DCA curve also showed that the combined model provided a higher net clinical benefit when compared to the clinical model and radiomics model. Therefore, it could be inferred that combining the clinic-radiological characteristics and radiomics features can improve the precision of predicting solitary-type IMA. This preoperative combined model has the potential to serve as a valuable tool for diagnosing IMA and supporting decision-making in therapeutic planning.

There were several limitations in this study. Firstly, this was a retrospective study and all the image data were collected from a single institution, which might have selection bias. Secondly, we obtained the medical imaging data of patients from different CT scanners, which might affect the radiomics analysis. It is important to take into account the variability in CT scanners and the consistent acquisition parameters in future studies. Thirdly, it is necessary to collect multicenter data to enlarge the sample size and conduct external validation to verify the generalization ability of our findings in the future.

In conclusion, the combined model integrating the clinic-radiological factors with radiomics features can be a noninvasive and effective new method for preoperatively diagnosing solitary-type IMA. This preoperative diagnosis will aid in decision-making support for therapeutic planning in cases of solitary-type IMA.

Abbreviations

IMA, invasive mucinous adenocarcinoma; INMA, invasive non-mucinous adenocarcinoma; CT, computed tomography; VOI, volume of interest; RFE, recursive feature elimination; LDA, linear discriminant analysis; LR-LASSO, logistic regression-least absolute shrinkage and selection operator; SVM, support vector machine; GLCM, gray level co-occurrence matrix; GLSZM, gray level size zone matrix; GLRLM, gray level run length matrix; NGTDM, neighboring gray tone difference matrix; GLDM, gray level dependence matrix; LoG, Laplacian of Gaussian; LBP, local binary pattern; PCC, Pearson correction coefficient; ROC, receiver operating characteristic; DCA, decision curve analysis; ACC, accuracy; SEN, sensitivity; SPE, specificity; PPV, positive predictive value; NPV, negative predictive value.

Author Contributions

All authors made a significant contribution to the work reported, whether that is in the conception, study design, execution, acquisition of data, analysis and interpretation, or in all these areas; took part in drafting, revising or critically reviewing the article; gave final approval of the version to be published; have agreed on the journal to which the article has been submitted; and agree to be accountable for all aspects of the work.

Funding

This work was supported by the Jiangsu Province Capability Improvement Project through Science, Technology and Education (Jiangsu Provincial Medical Key Discipline Cultivation Unit) (No. JSDW202242).

Disclosure

The author(s) report no conflicts of interest in this work.

References

1. Succony L, Rassl DM, Barker AP, McCaughan FM, Rintoul RC. Adenocarcinoma spectrum lesions of the lung: detection, pathology and treatment strategies. *Cancer Treat Rev*. 2021;99:102237. doi:10.1016/j.ctrv.2021.102237
2. Travis WD, Brambilla E, Nicholson AG, et al. The 2015 world health organization classification of lung tumors: impact of genetic, clinical and radiologic advances since the 2004 classification. *J Thorac Oncol*. 2015;10(9):1243–1260. doi:10.1097/jto.0000000000000630
3. Nicholson AG, Tsao MS, Beasley MB, et al. The 2021 WHO classification of lung tumors: impact of advances since 2015. *J Thorac Oncol*. 2022;17(3):362–387. doi:10.1016/j.jtho.2021.11.003
4. Chang JC, Offin M, Falcon C, et al. Comprehensive molecular and clinicopathologic analysis of 200 pulmonary invasive mucinous adenocarcinomas identifies distinct characteristics of molecular subtypes. *Clin Cancer Res*. 2021;27(14):4066–4076. doi:10.1158/1078-0432.Ccr-21-0423
5. Xu L, Li C, Lu H. Invasive mucinous adenocarcinoma of the lung. *Transl Cancer Res*. 2019;8(8):2924–2932. doi:10.21037/tcr.2019.11.02
6. Chang WC, Zhang YZ, Nicholson AG. Pulmonary invasive mucinous adenocarcinoma. *Histopathology*. 2024;84(1):18–31. doi:10.1111/his.15064
7. Matsui T, Sakakura N, Koyama S, et al. Comparison of surgical outcomes between invasive mucinous and non-mucinous lung adenocarcinoma. *Ann Thorac Surg*. 2021;112(4):1118–1126. doi:10.1016/j.athoracsur.2020.09.042
8. Lee MA, Kang J, Lee HY, et al. Spread through air spaces (STAS) in invasive mucinous adenocarcinoma of the lung: incidence, prognostic impact, and prediction based on clinicoradiologic factors. *Thorac Cancer*. 2020;11(11):3145–3154. doi:10.1111/1759-7714.13632
9. Cha YJ, Shim HS. Biology of invasive mucinous adenocarcinoma of the lung. *Transl Lung Cancer Res*. 2017;6(5):508–512. doi:10.21037/tlcr.2017.06.10
10. Sun X, Zeng B, Tan X, Chen Z, Pan X, Jiang L. Invasive mucinous adenocarcinoma of the lung: clinicopathological features, (18)F-FDG PET/CT findings, and survival outcomes. *Ann Nucl Med*. 2023;37(3):198–207. doi:10.1007/s12149-022-01816-7
11. Nie K, Nie W, Zhang YX, Yu H. Comparing clinicopathological features and prognosis of primary pulmonary invasive mucinous adenocarcinoma based on computed tomography findings. *Cancer Imag*. 2019;19(1):47. doi:10.1186/s40644-019-0236-2
12. Kim DH, Bae SY, Na KJ, et al. Radiological and clinical features of screening-detected pulmonary invasive mucinous adenocarcinoma. *Interact Cardiovasc Thorac Surg*. 2022;34(2):229–235. doi:10.1093/icvts/ivab257
13. Watanabe H, Saito H, Yokose T, et al. Relation between thin-section computed tomography and clinical findings of mucinous adenocarcinoma. *Ann Thorac Surg*. 2015;99(3):975–981. doi:10.1016/j.athoracsur.2014.10.065
14. Wang T, Yang Y, Liu X, et al. Primary invasive mucinous adenocarcinoma of the lung: prognostic value of CT imaging features combined with clinical factors. *Korean J Radiol*. 2021;22(4):652–662. doi:10.3348/kjr.2020.0454
15. Zong Q, Zhu F, Wu S, et al. Advanced pneumonic type of lung adenocarcinoma: survival predictors and treatment efficacy of the tumor. *Tumori*. 2021;107(3):216–225. doi:10.1177/0300891620947159
16. Miyamoto A, Kurosaki A, Fujii T, Kishi K, Homma S. HRCT features of surgically resected invasive mucinous adenocarcinoma associated with interstitial pneumonia. *Respirology*. 2017;22(4):735–743. doi:10.1111/resp.12947
17. Miyata N, Endo M, Nakajima T, et al. High-resolution computed tomography findings of early mucinous adenocarcinomas and their pathologic characteristics in 22 surgically resected cases. *Eur J Radiol*. 2015;84(5):993–997. doi:10.1016/j.ejrad.2015.01.014
18. Zhang X, Qiao W, Kang Z, et al. CT features of stage IA invasive mucinous adenocarcinoma of the lung and establishment of a prediction model. *Int J Gene Med*. 2022;15:5455–5463. doi:10.2147/ijgm.S368344
19. Lambin P, Leijenaar RTH, Deist TM, et al. Radiomics: the bridge between medical imaging and personalized medicine. *Nat Rev Clin Oncol*. 2017;14(12):749–762. doi:10.1038/nrclinonc.2017.141
20. Wu G, Woodruff HC, Shen J, et al. Diagnosis of invasive lung adenocarcinoma based on chest ct radiomic features of part-solid pulmonary nodules: a multicenter study. *Radiology*. 2020;297(2):451–458. doi:10.1148/radiol.2020192431
21. Park S, Lee SM, Noh HN, et al. Differentiation of predominant subtypes of lung adenocarcinoma using a quantitative radiomics approach on CT. *Eur Radiol*. 2020;30(9):4883–4892. doi:10.1007/s00330-020-06805-w
22. Traverso A, Kazmierski M, Zhovannik I, et al. Machine learning helps identifying volume-confounding effects in radiomics. *Phys Med*. 2020;71:24–30. doi:10.1016/j.ejmp.2020.02.010
23. Koo TK, Li MY. A guideline of selecting and reporting intraclass correlation coefficients for reliability research. *J Chiropr Med*. 2016;15(2):155–163. doi:10.1016/j.jcm.2016.02.012
24. Song Y, Zhang J, Zhang YD, et al. FeAture Explorer (FAE): a tool for developing and comparing radiomics models. *PLoS One*. 2020;15(8):e0237587. doi:10.1371/journal.pone.0237587

25. Sala E, Mema E, Himoto Y, et al. Unravelling tumour heterogeneity using next-generation imaging: radiomics, radiogenomics, and habitat imaging. *Clin Radiol*. 2017;72(1):3–10. doi:10.1016/j.crad.2016.09.013
26. Yang C, Chen W, Gong G, Li Z, Qiu Q, Yin Y. Application of CT radiomics features to predict the EGFR mutation status and therapeutic sensitivity to TKIs of advanced lung adenocarcinoma. *Transl Cancer Res*. 2020;9(11):6683–6690. doi:10.21037/tcr-20-1216
27. Wen Q, Yang Z, Dai H, Feng A, Li Q. Radiomics study for predicting the expression of pd-l1 and tumor mutation burden in non-small cell lung cancer based on ct images and clinicopathological features. *Front Oncol*. 2021;11:620246. doi:10.3389/fonc.2021.620246
28. Qiu Q, Xing L, Wang Y, Feng A, Wen Q. Development and validation of a radiomics nomogram using computed tomography for differentiating immune checkpoint inhibitor-related pneumonitis from radiation pneumonitis for patients with non-small cell lung cancer. *Front Immunol*. 2022;13:870842. doi:10.3389/fimmu.2022.870842
29. Zhang J, Hao L, Li M, Xu Q, Shi G. CT radiomics combined with clinicopathological features to predict invasive mucinous adenocarcinoma in patients with lung adenocarcinoma. *Technol Cancer Res Treat*. 2023;22:15330338231174306. doi:10.1177/15330338231174306
30. Zhang J, Hao L, Qi M, et al. Radiomics nomogram for preoperative differentiation of pulmonary mucinous adenocarcinoma from tuberculoma in solitary pulmonary solid nodules. *BMC Cancer*. 2023;23(1):261. doi:10.1186/s12885-023-10734-4
31. Kakino R, Nakamura M, Mitsuyoshi T, et al. Comparison of radiomic features in diagnostic CT images with and without contrast enhancement in the delayed phase for NSCLC patients. *Phys Med*. 2020;69:176–182. doi:10.1016/j.ejmp.2019.12.019
32. Qian Z, Li Y, Wang Y, et al. Differentiation of glioblastoma from solitary brain metastases using radiomic machine-learning classifiers. *Cancer Lett*. 2019;451:128–135. doi:10.1016/j.canlet.2019.02.054
33. Shen Y, Xu F, Zhu W, Hu H, Chen T, Li Q. Multiclassifier fusion based on radiomics features for the prediction of benign and malignant primary pulmonary solid nodules. *Ann Translat Med*. 2020;8(5):171. doi:10.21037/atm.2020.01.135
34. Avanzo M, Wei L, Stancanello J, et al. Machine and deep learning methods for radiomics. *Med Phys*. 2020;47(5):e185–e202. doi:10.1002/mp.13678
35. Ubaldi L, Valenti V, Borgese RF, et al. Strategies to develop radiomics and machine learning models for lung cancer stage and histology prediction using small data samples. *Phys Med*. 2021;90:13–22. doi:10.1016/j.ejmp.2021.08.015
36. Erickson BJ, Korfiatis P, Akkus Z, Kline TL. Machine Learning for Medical Imaging. *Radiographics*. 2017;37(2):505–515. doi:10.1148/rg.2017160130
37. Liu J, Zeng P, Guo W, et al. Prediction of high-risk cytogenetic status in multiple myeloma based on magnetic resonance imaging: utility of radiomics and comparison of machine learning methods. *J Magn Reson Imaging*. 2021;54(4):1303–1311. doi:10.1002/jmri.27637
38. Azour L, Ko JP, O'Donnell T, Patel N, Bhattacharji P, Moore WH. Combined whole-lesion radiomic and iodine analysis for differentiation of pulmonary tumors. *Sci Rep*. 2022;12(1):11813. doi:10.1038/s41598-022-15351-y
39. Song F, Song X, Feng Y, et al. Radiomics feature analysis and model research for predicting histopathological subtypes of non-small cell lung cancer on CT images: a multi-dataset study. *Med Phys*. 2023;50(7):4351–4365. doi:10.1002/mp.16233